NO x pathways in lean partially premixed swirling H2-air turbulent flame

T. Capurso, D. Laera, E. Riber, B. Cuenot

NO_x pathways in lean technically premixed swirling H2-air turbulent flame

T. Capurso[a,b,c,*], D. Laera[a,b], E. Riber[b], B. Cuenot[b]

[a] *Department of Mechanics, Mathematics and Management - Polytechnic University of Bari, Via Re David, 200, 70125 Bari, Italy*
[b] *CERFACS, 42 avenue Gaspard Coriolis, 31057 Toulouse, France*
[c] *Arts et Metiers Institute of Technology, CNAM, LIFSE, ENSAM University, 75013 Paris, France*

Abstract

Today's climate and energy challenges are pushing the use of decarbonised and renewable alternative fuels in the field of power generation and transportation. Hydrogen as a fuel is a good candidate to meet these requirements since it offers no-carbon emissions and can play the role of energy vector to store energy in excess produced by renewable energy. Nonetheless, NO_x production needs to be assessed. For this reason, high-fidelity LES simulations of a 3D partially premixed turbulent flame, whose experiments have been performed at the Berlin Institute of Technology (TUB) are proposed accounting for NO_x production. To properly capture the right level of NO_x, a new skeletal kinetic scheme for air-H2 combustion (15 species and 47 reactions) has been developed on purpose taking into account all the NO_x pathways. With the purpose to accurately solve the combustion process and the NO_x production level, the static mesh refinement (SMR) and the conju-

*Corresponding author
Email address: tommaso.capurso@poliba.it (T. Capurso)

gate heat transfer (CHT) techniques have been applied and their impact on the numerical solution are discussed. A detailed analysis of the preferential diffusion and NO formation is presented proving that the numerical model for 3D turbulent flame including complex transport phenomena and the new H2Air_15_47_TC chemical kinetic scheme is able to predict the NO dynamic formation accounting for the primary and secondary routes: N_2O and NNH.
Keywords: Hydrogen/air combustion, NO_x, Large Eddy Simulation, Reduced chemistry, Conjugate Heat Transfer

---

1. Introduction

Hydrogen (H_2) is nowadays considered as the most promising technical solution to reach European Union goal of zero-net CO_2 emissions by 2050, opening a new era of decarbonized combustion [1]. Nevertheless, even if H_2 does not contribute through chemical reactions to CO_2 emissions, its chain of reactions leads to the production of nitrogen oxides, mainly NO, NO_2 and N_2O. In the last decades, a lot of work has been devoted to the study of N-gases since they are responsible of air pollution and global warming. Indeed, N_2O is a strong and long lifetime greenhouse gases (GHG) representing 7% of GHG produced in Europe with an increasing rate of 2% per decade [2]. In addition, in combustion systems N_2O is a precursor of the other NO_x through reactions $N_2O+O \Longleftrightarrow NO+NO$ and $N_2O+H \Longleftrightarrow NO+NH$ [3]. Elevated levels of NO and NO_2 are the cause of tropospheric ozone formation and acidification of the atmosphere [4]. From this scenario, clearly appears that an intense use of hydrogen as fuel in combustion systems calls for a full understanding of the formation mechanism responsible of these pollu-

tants with the objective of designing novel injectors able to moderate their emissions. Developments are also required for numerical tools that must ensure accurate prediction standards, thus increasing their potential as a complement to experimental analyses. The present article deals with these challenges by proposing a high-fidelity numerical analysis of NO_x production by a turbulent lean partially premixed swirling hydrogen-air flame.

The study of NO_x production and destruction after combustion of different fuels in oxygen-nitrogen mixtures pones its basis in the last century. Herein a brief summary of the study on NO reactions, which is not intended to be exhaustive of all the literature, is proposed. Zeldovich [5] was the first to clarify the thermal character of the NO formation in combustion and explosion. Homer et al. [6] investigated the importance of oxygen atom overshoot close to the flame front and the additional HO_2 route to improve the modeling of NO at high temperature. Glarborg et al. [7] proposed a comprehensive reaction scheme for NO_x prediction based on carbon fuels studies. A large variety of experiments and new models have been carried out on hydrogen laminar flames to investigate the primary sources of NO_x production, e.g. Refs. [8], but also its secondary routes which are important when the thermal NO emissions are mitigated [9]. In the last decade of the last century, more attention has been paid to secondary routes since they actively participate in lean and low temperature combustion. For instance, Bozzelli et al. [10] proposed the NNH route for the first time also investigating its link with the N_2O pathways. Since then, other studies have been done on NNH radical for instance the importance of nitrogen abstraction from NNH at high temperatures [11]. Recently, the NNH mechanism for lean hydrogen flames

has been discussed by Purohit et al. [12]. Glarborg [13] recently reviewed the NO modeling state of the art highlighting the importance of N_2O and NNH routes, and showing the reasons why this topic is still a great challenge in the community. Recently, Durocher et al. [14] demonstrated experimentally that the modern detailed kinetic mechanisms present in the literature are now able to describe with fewer uncertainties the N_2O and NNH pathways. Focusing on hydrogen, few experimental studies have been performed in gas turbines configurations for multiple injector designs in order to evaluate the impact of lean hydrogen combustion on NO_x production. The impact of small hydrogen addition in the NO_x levels produced by methane-air flame was at first investigated for classical Dry Low NO_x systems [15]. Recently, similar studies have been also performed in the MIRADAS test rig developed at IMFT laboratory where a separate injection of small quantity of hydrogen has been proved to be able to stabilize a thermo-acoustically unstable flame with, however, a negative impact on NO_x levels [16]. Partially premixed hydrogen-air flames have been also investigated in the last years by the research group of the Berlin Institute of Technology (TUB) [17] with the aim of designing injectors able to resist flashback inclination while keeping low levels of NO_x (<10 ppm NO_x at 15%O_2) [17]. Similar objectives have also driven the developments of novel designs as the micro-mixing injector proposed by Tekin et al. [18].

For what concerns the numerical investigations, a variety of Direct Numerical Simulations (DNS) can be found in literature focusing on H_2 flames. Rieth et al. [19] pointed out the importance of preferential diffusion in hydrogen air flame even at $Ka \gg 1$, in which the species molecular diffusion

is usually neglected. Aspden et al. [20] studied lean hydrogen combustion, ϕ=0.4, by varying the Ka number showing how high turbulent flames disassociate heat release rate and fuel consumption. DNS of turbulent swirled imposed premixed flames have been performed in the past to investigate the structure of the recirculation zones and the mechanisms of reaction. Minamoto et al. [21] showed a correlation between reaction rates and both scalar gradient and small turbulence structures. Aoki et al. [22] investigated the impact of strain on the heat release rate at different swirl numbers. None of aforementioned works focuses on pollutants predictions. Only few DNS simulations focused on NO formation. For instance, Bell et al. [23] focused on the development of cellular burning patterns for very lean hydrogen combustion and how these impact on NO production. In addition, Netzer et al. [24] analyzed the impact of hydrogen preferential diffusion and NO formation for lean-to-rich ammonia/hydrogen/nitrogen-air flames.

When it comes to complex configurations, Large Eddy Simulations (LES) have also been extensively used in the recent years providing detailed understanding of the coupling between elementary physical processes involved in the combustion of complex flames at reasonable computational cost. Focusing on hydrogen applications, most studies have been performed considering H_2 diluted with conventional fuels. Gadalla et al. [25] analyzed by LES the impact of tri-fuel (diesel-methanol-hydrogen) combustion for marine applications. For what concerns methane enrichment with hydrogen, e.g., Laera et al. [26] focused on the stabilization of CH_4 flames with H_2 injection, Agostinelli et al. [27] studied the impact of H_2-enrichment on the flame structure and combustion dynamics of a CH_4-air swirling flame, and Afarin

et al. [28] investigated methane/hydrogen mixtures in MILD regime. Also ammonia blended with hydrogen has been studied with particular attention to the NO production [29]. To the authors knowledge, LES analyses carried out on pure hydrogen-air swirling flames are very limited. Mira et al. [30] investigated the injector developed at TUB addressing the capacity of flamelet combustion model to predict perfectly premixed hydrogen-air mixture under adiabatic stable flame conditions. Nevertheless, no investigations on NO_x emissions were proposed. Only few LES works focused on NO_x estimation for gas turbine application. For instance, Meloni et al. [31] proposed LES simulation with the transport of a source term for the prediction of NO_x.

The present work aims at filling this gap by performing high-fidelity LES of a complex 3D lean partially premixed swirling hydrogen-air flame including transport phenomena with the aim to correctly evaluate NO_x emissions. In particular, the main sources of NO production and the impact of heat losses on N_2O, which is detrimental product of hydrogen combustion, will be presented. This work refers to experiments performed in a technically premixed burner at the laboratory scale rig operated at TUB. To accurately predict the NO_x production, a novel skeletal chemical scheme for hydrogen oxidation with NO_x formation (15 species and 47 reactions - H2Air_15_47_TC) is derived and validated against detailed mechanisms and experiments. The most important reactions and links have been preservated, moreover the skeletal mechanism has been validated on a wide range of operating conditions to be as general as possible. The resulting skeletal chemical scheme is then included in the compressible parallel code AVBP (`http://www.cerfacs.fr/avbp7x/`) in which turbulent combustion is handled by the dynamic formulation of the

Thickened Flame LES combustion model (TFLES) [32]. To account for the effect of heat transfer on flame stabilization and NO_x formation, Conjugate Heat Transfer (CHT) simulations are performed by coupling the AVBP LES solver with the AVTP heat-conduction solver [33]. Finally, the static mesh refinement (SMR) technique is also applied to correctly resolve the flame front. The article is organized as follows: the experimental test rig is presented in section 2. The numerical methods (i.e., SMR, CHT and ARC chemistry) applied to correctly solve the turbulent hydrogen-air flame are described in section 3. Finally, section 4 shows the results for both the isothermal and reactive cases with a focus on compressibility effects, air/fuel mixing, flame stabilization, heat losses and NO_x formation mechanisms.

2. Experimental Setup : TUB rig

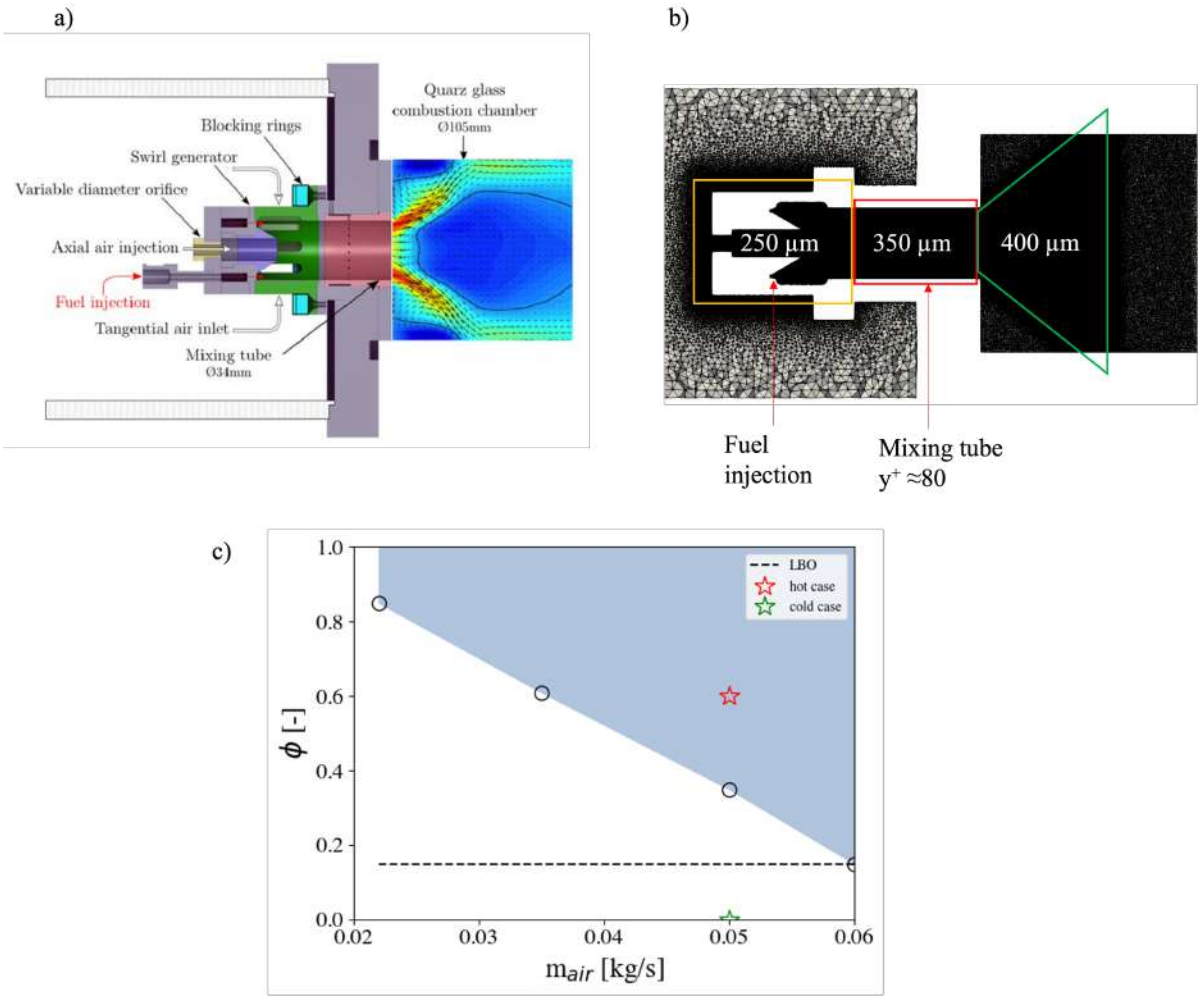

Figure 1: a) Berlin Institute of Technology experimental test rig [17]; b) numerical domain and grid with refinement boxes; c) Stable flame region colored in light-blue.

The present numerical analysis refers to experimental measurements performed in the laboratory scale combustor developed at TUB shown in Fig. 1(a) [17]. This rig has been originally designed to study hydrogen (and syngas with

high hydrogen content) swirling flames at ambient pressure. Pre-heated air at $T_{air} = 453$ K is injected through a large plenum and then it is split in two separate jets: a first portion flows through an orifice (d_o) creating a central air jet whose high momentum is functional in avoiding flashback. The remaining portion enters the mixing tube through a radial swirler (Fig.1(b)). The air splitting is adjustable by changing the dimension of d_o and it is quantified by the parameter χ, defined as follows:

$$\chi = \frac{Q_{ax}}{Q_{sw} + Q_{ax}} \tag{1}$$

where Q_{ax} (m^3/s) stands for the flow rate entering the orifice and Q_{sw}, the remaining part, which flows through the swirler. Unfortunately, no detailed measurements of χ are available. The swirl number/intensity can be controlled by moving the blocking rings highlighted in Fig.1(a). Subsonic hydrogen at $T_{fuel} = 320$ K is axially injected at roughly 400 m/s by 16 small pipes (d_f=0.8 mm) circumferentially arranged at the bottom of the mixing tube, Fig.1(b). The two air flows meet each other in the mixing tube, which is an axial pipe of length 60 mm and diameter 34 mm. In this region the flow has an average bulk velocity of 70 m/s and Re=75000.

A circular combustion chamber with diameter d_{cc}=105 mm and length $8.8 \times d_{cc}$ is mounted at the end of the mixing tube. A large experimental campaign has been performed on this burner by varying a great variety of parameters: the orifice diameter, the air and fuel flow rates ($J = \rho_{fuel} u_{fuel}^2 / \rho_{air} u_{air}^2$), the fluids temperature and the swirl number (S_w). For moderate axial air injection, namely d_o=8.0 mm and swirl number equal to 0.9, the burner is characterized by a stable flame region represented in light blue in Fig. 1(c). This graph is marked off by stoichiometric conditions at the top and by the

Lean Blowout (LBO) condition ($\phi \approx$0.15, dashed line) at the bottom.

In this work, two operating conditions have been investigated: first, a cold flow point, indicated with a green star in Fig. 1(c), and, then, a stable flame configuration marked by the red star in the same figure. The latter is characterized by a global equivalence ratio ϕ=0.6, which corresponds to a fuel/air momentum ratio J=2.4 and a thermal power output P_{th}=105 kW.

3. Numerical model and methods

High-fidelity LES have been performed using the AVBP code solving the compressible Navier-Stokes multi-species equations. The SIGMA subgrid-scale model is used [34] for turbulent closure. The third-order accurate Taylor-Galerkin (TGCC) scheme is used for the discretization of the convective terms with Colin et al. [35] artificial viscosity model. The turbulent flame is solved by the dynamic version of the thickened flame model (DTFLES) [32]: thickening is generally applied everywhere a reactive zone is detected by a flame sensor modelled as a function of the fuel consumption rate [36] and the thickening factor is adapted depending on the local mixture properties and grid size, to ensure sufficient resolution. Typically the thermal flame thickness (δ_T) is described with at least seven points when using semi-detailed kinetic schemes [37]. To retrieve the correct chemistry/turbulence interaction, the Charlette efficiency function has been used with a constant coefficient β=0.5 [38]. Being partially premixed flames characterised by both premix and diffusion regions [39], DTFLES has been further conditioned using the Takeno Index [40]: thickening is deactivated in diffusion flame zones, being the TFLES formalism and the efficiency functions formally applicable

only to premixed flames [32]. As explained in [41], diffusion flames naturally adapt to coarse meshes and in the high Damköler regime, their consumption speed is controlled by the turbulent fluxes.

The numerical domain is shown in Fig. 1(b). Few simplifications have been performed with respect to the actual rig geometry. Fuel line is simplified as 16 small pipes delivering uniformly distributed fuel mass flow. In the real case a non-uniform fuel injection from each hole can be expected. Following previous work on the same configuration [30], the 24 dilution holes presented in the original design close to the combustion chamber inlet to avoid boundary layer flashback have been also discarded to reduce the computational cost, since the total air flow rate passing through them is estimated to be below 2%.

For the non-reactive simulations the numerical domain is discretized with an unstructured mesh of 126 million cells with local refinement as depicted in Fig. 1(b). Inlet and outlet boundary conditions are treated with the Navier-Stokes Characteristic Boundary Conditions (NSCBC) [42] with a relaxation factor k=1000 s^{-1} imposed on air and fuel inlets. For the non-reactive case, all the walls are set no-slip and adiabatic, apart from the mixing tube walls, where the grid size used returned a $y^+ \approx 80$. For those, a wall-model (high-Reynolds approach) for imposing the wall shear stress is applied [43].

3.1. Static Mesh Refinement

Differently from cold simulations, Static Mesh Refinement (SMR) approach is employed in reactive simulations to improve flame resolutions containing computational cost. To this scope, the SMR flame criterion proposed by Agostinelli et al. [44] for CH_4 combustion was extended to a pure hydro-

gen configuration. It resides on the rationale of a refinement metric based on the definition of a flame probability function, i.e., a statistically relevant region of interest (ROI) in which the grid can be modified. Resolution is controlled by imposing a maximum effective thickening factor resulting from the combination of its mean value and variance. In the present configuration, target thickening factor is set equal to 4, resulting in the 149 million cells with minimum cell dimension of Δx=200 μm shown in Fig. 2(a). No mesh coarsening is applied in this case, since the volume already refines overlap regions of flow physics interest.

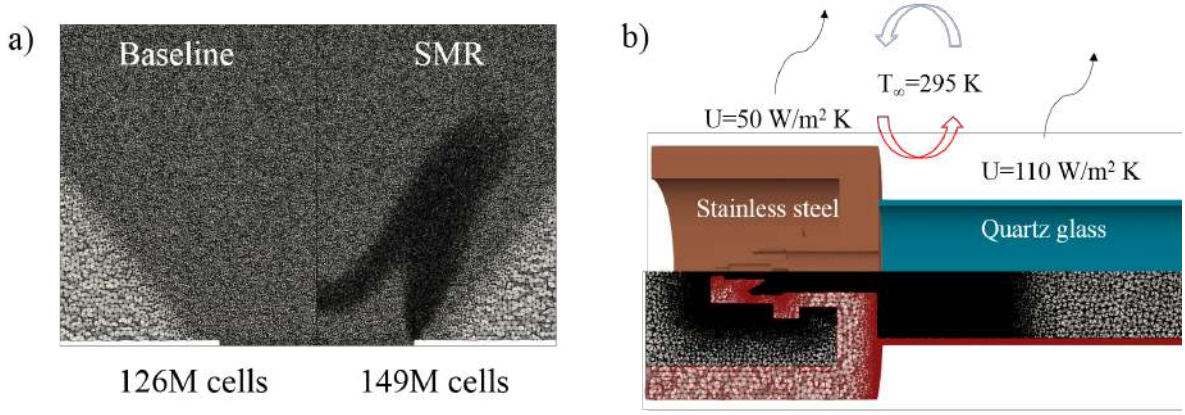

Figure 2: a) Comparison of the two computational grids: baseline for non reactive simulations (left), and the final grid with the SMR for reactive simulations (right); b) Longitudinal view of the fluid (black edges) and solid domains (red edges) reproducing the experimental test rig where boundary conditions, materials and grid are highlighted.

3.2. Conjugate heat transfer

In the present study, the impact of heat transfer on flame anchoring, temperature pattern and NO_x production is investigated. Conjugate heat transfer technique is applied to take into account the correct level of heat

transfer from the hot gases to the solid and then towards the external ambient. This technique has been recently demonstrated to be more accurate than the heat resistance tuning at cost of increasing the computational time [39]. To this scope, the LES solver AVBP is coupled with AVTP [33, 45], a solver developed at CERFACS, which solves the thermal conduction problem. To couple the two solvers, the Parallel Coupling Strategy has been developed on the basis of CWIPI libraries [46]. A 7 million cells computational mesh has been generated for the solid part of the burner guaranteeing at least 5 points in the wall thickness (Fig. 2(b)). In absence of experimental measurements on the walls, a first attempt for the thermal boundary conditions on the walls has been made by evaluating the heat fluxes. The heat flux per unit of surface (W/m^2) is calculated as follows:

$$\dot{q} = U(T - T_\infty) \tag{2}$$

with the T_∞ imposed as the ambient temperature and U, the heat transfer coefficient (W/m^2K). In the most general case, the latter is evaluated as the combination of the conduction, convection and radiation heat transfer coefficients. Following the thermal-electric analogy [1], the conduction heat transfer term is in series with an equivalent heat transfer calculated as if the convective and the radiation heat transfer terms were in parallel. In this work, the conduction problem is solved by AVTP, thus on the external surfaces of the solid, the heat transfer coefficient has been evaluated as the combination of the natural convection on horizontal surfaces and radiation

[1] Temperature difference as the electric potential (V) and the reciprocate of the resistance ($1/R$) as the heat transfer coefficient.

heat transfer, thus U is expressed as follows:

$$\frac{1}{U} = \left(\frac{1}{h_{conv} + h_{rad}} \right) \tag{3}$$

The convection heat transfer coefficient, h_{conv}, is based on the Rayleigh number, an adimensional number function of the surface shape and orientation. For instance, for natural convection around a horizontal cylinder, h_{conv} can be calculated as:

$$h_{conv} = \frac{k}{D} \left(0.6 + \frac{0.387 Ra_D^{1/6}}{(1 + (0.559/Pr)^{9/16})^{8/27}} \right)^2 \tag{4}$$

where Ra and Pr are the Rayleigh and the Prandtl number, respectively. The last term on the right hand side of Eq. (4) is calculated as: $h_{rad} = 1/[\sigma\epsilon(T^4 - T_\infty^4)/(T - T_\infty)]$. The values of the heat transfer coefficients for the external combustion chamber and plenum walls are sets to 110 and 50 W/m^{2}K, respectively. For the reactive case, the wall law coupled loss boundary condition has been applied to the combustion chamber and the backplane. This boundary defines a wall with heat-loss using a wall-model (high-Reynolds approach) to impose wall shear stress and wall heat flux.

AVBP and AVTP run in parallel and exchange the solid surface temperature T_s and the heat flux $\dot{q}$ at the boundaries. The characteristic time of the fluid (τ_f) and solid (τ_s) problems are different, i.e., $\tau_s \approx 100\ \tau_f$, hence the temporal coupling consists in running the LES solver for approximately 100 iterations and then running 1 iteration for the conductive problem.

3.3. Reduced scheme for H2-air with NO_x

In the field of numerical simulations, a big challenge is to employ as accurate as possible chemical kinetic schemes. The number of species transported

is usually kept low to control the computational time. For this purpose, a new skeletal scheme for hydrogen-air combustion including NO_x prediction has been proposed. Hydrogen combustion has been widely investigated since the last century in the context of oxy-fuel rocket propulsion applications. It is a light molecule with high molecular diffusivity resulting in a very low Lewis number, Le=0.3, if compared to classical hydrocarbons in which $Le \approx 1$ [47]. Additionally, the thermophoresis (or Soret effect) becomes relevant for hydrogen in low velocity zones in presence of temperature gradient [48]. From a modelling point of view, the kinetic species and reactions behind the combustion of hydrogen are well-known and studied, since they could be found as sub-mechanisms of all the hydrocarbon chemistries, e.g., methane and propane [49]. A large number of these detailed schemes developed for hydrocarbons and syngas could be found in literature, e.g., Gri-Mech3.0 [50], Polimi (CRECK modeling group) [51] and Galway NUIGMech1.1 [52], which have been recently integrated in the optimized C3MechV3.3 [53]. All of these well describe hydrogen/air oxidation and, also, NO_x chemistry. Despite the high precision, none of the aforementioned schemes is suitable to be directly used in a CFD code. Indeed, the computational cost of accounting for more than 30 species and thousands of reactions (some of them characterized by very small characteristic time) would make the numerical simulation unsustainable. Reduced mechanisms are required to this scope. Few examples for hydrogen-air are the San Diego [54] (21 species and 40 reactions) and the Boivin [55] (skeletal with 9 species and 12 reactions) mechanisms. Both are widely employed in CFD since they provide a good compromise between accuracy of the results and computational costs. Although a kinetic scheme

including NO_x [56] (15 species and 58 reactions) has been proposed for very lean mixtures, this has not been validated against canonical experimental flames and never applied to a real gas turbine burner. Here a new hydrogen-air skeletal mechanism is proposed (H2Air_15_47_TC), that includes the NO branches to respond to the demand of numerical computations capable of predicting the impact of H_2-air combustion in real combustion applications. The skeletal mechanism here proposed has been validated and it is indicated as a generic-purpose scheme for a broad range of operating conditions (different operating equivalence ratios, temperatures and pressures). Based on the experimental activity carried out on hydrogen flames, the ways to produce NO_x can be sum up in 3 categories: the thermal path defined by Zel'dovich sub-mechanism, the N_2O intermediate path and finally the secondary route through diazenyl radicals (NNH). Thermal NO_x are mainly controlled by combustion temperature since the initiation reaction $O + N_2 \Longleftrightarrow NO + N$ involves elevated energy of activation. The N_2O intermediate chemistry is, on the contrary, little sensitive to temperature because it is led by a third body reaction which necessitates low energy of activation [9]. Therefore, the N_2O route is promoted at low temperature, lean condition and slightly at high pressure. Finally, the NNH route is promoted in the flame front and controlled by the radicals O and H. Another important aspect to underline is the link between NNH and N_2O:

$$NNH + O \Longleftrightarrow N_2O + H \tag{5}$$

The skeletal mechanism was obtained with the ARCANE code co-developed by CERFACS and Cornell University [57]. It is a fully automatic multi-step

reduction tool relying on DRGEP [58], chemical lumping [59] and Quasi-Steady State Assumption [60]. CRECK detailed mechanism [51], which comprises 159 species and 2459 reactions was chosen as a reference for this work because of its extensive use in the community. An error of 5% is set as a limit for the ignition time delay as well as for the laminar flame speed, whereas, a maximum error of 1% has been imposed on the integral value of NO. The reduction process, which targets chains for the production of NO via N_2O and NNH secondary routes, returns a skeletal scheme with 15 species and only 47 reactions. The set of species and reactions can be consulted in the Supplementary Material. It is important to highlight that in the reduction process, the O and H radicals have been set as main targets being central for the O_2/H_2 and NO oxidation pathways.

Cantera predictions (www.cantera.org) [61] of laminar flame speed of an unstrained premixed flame on a wide range of pressures and temperatures conditions are shown in Fig. 3(a-b-c). The calculations have been carried out by activating the detailed transport (multi-species) method and the Soret effect. Results with the reduced scheme are compared to the detailed CRECK and the skeletal scheme of Boivin et al. [55] as a benchmark. A good agreement is observed between the detailed and the new skeletal schemes, whereas some discrepancies can be observed with the existing skeletal scheme (Boivin) without NO_x [55] especially at pressures far from the atmospheric pressure (Fig. 3(a)) and high temperatures (Fig. 3(c)).

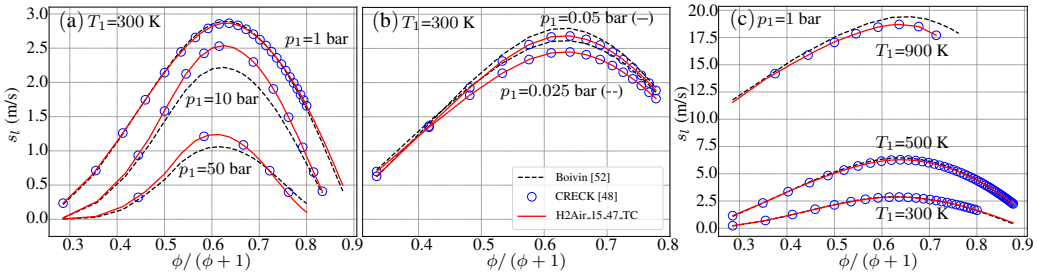

Figure 3: Comparison of laminar flames speed calculated with detailed transport (multi-species) for detailed scheme (blue circles) [51], Boivin skeletal scheme (black) [55] and H2Air_15_47_TC skeletal scheme (red) at elevated pressure (a), low pressure (b) and elevated temperatures at constant pressure p_1=1 bar (c).

A further comparison has been performed between the detailed scheme and the new skeletal mechanism in terms of NO mass fraction. In the Supplementary Material, graphs representing three 1D canonical premixed flame at different equivalence ratios, pressures and temperatures are plotted. This plots confirm the effectiveness of the reduction process. Finally the H2Air_15_47_TC scheme has been validated on experiments performed on laminar diffusion flames (Re=400) diluted with inert at constant strain rate a=100 s^{-1} [8]. Two counterflow flames with a global equivalence ratio of ϕ =0.9 & 1.4, and same strain rate as in the experiments, were computed in Cantera. In Fig. 4(a) the lean case has been calculated also with the Gri-Mech 3.0 and 2.11 [50, 62], and the Galway schemes. The two Gri-Mech mechanisms over-predict the width and the peak of the NO profile, which instead is well captured by CRECK and the new skeletal scheme, herein proposed. The Galway resolves accurately the maximum value, but shows a second ripple which is not evidenced by experiments. Furthermore, when the Soret effect is activated in the rich case (Fig. 4(b)) a slight over-prediction

of the NO concentration is noted. This effect is present in both detailed (CRECK) and skeletal (H2Air_15_47_TC) mechanisms, thus it does not directly depend on the reduction procedure. Nevertheless, the proposed scheme correctly reproduces NO experimental profiles [8].

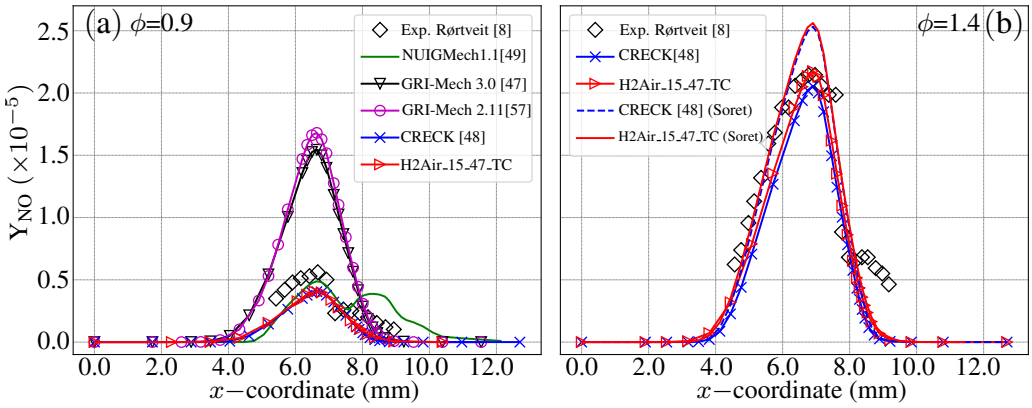

Figure 4: NO profiles (a-b) calculated for counterflow flames and compared with experimental data [8] at fixed $p = 1$ bar, $T = 300$ K and strain a=100 s^{-1}.

Once validated, NO formation routes can be investigated using this skeletal mechanics for the global operating condition of $\phi = 0.6$. A 1D premixed unstretched flame has been calculated in Cantera and its reaction paths are shown in Fig. 4. This graph shows the fluxes of the element according to their net reaction rates. The numbers associated to the single path are the reaction rates fluxes normalized to the highest value in the graph. Moreover, for each path, the species involved in the reactions are noted.

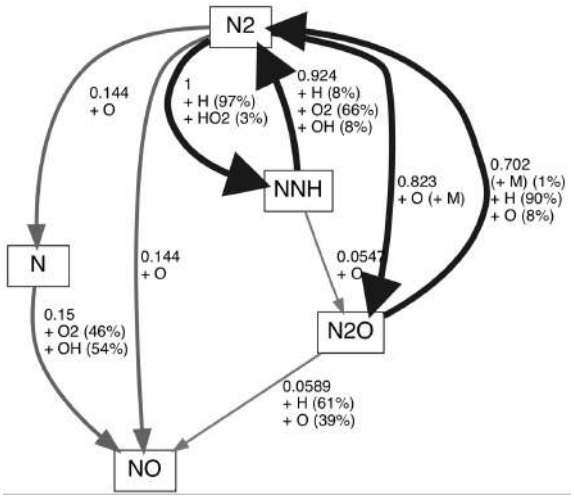

Figure 5: The reaction paths for an hydrogen flame at $T_{ad} \approx 1900$ K using the skeletal mechanism, where the arrow thickness stands for normalized fluxes of the reaction rate (where 1 is the maximum).

Looking at Fig. 5, it is noted that the N_2 oxidation to NO is initiated through different routes. Leaving out the thermal path for simplicity, one of others is the NNH, which is then converted to N_2O and finally to NO. Also the abstraction of hydrogen atom from NNH reconstructing N_2 and destroying NNH seems remarkable as introduced by [11]. Another path is the direct nitrous oxide way. The first step of both ways (NNH and N_2O) is characterized by an evident back and forth reaction. Conversely, it is worth to emphasize that the reactions between NNH and N_2O and finally from N_2O to N_2 are marked by a one direction behavior, even if they are bidirectional by nature. These results are in accordance with Skotenne et al. [9] and further confirmed in experiments proposed by Purohit et al. [12] on lean-hydrogen combustion. The reduction process was therefore able to preserve important reactions for the final NO production, refer to Supplementary Material, as

well as the link between the secondary routes which, on the contrary, are absent in the Gri-Mech mechanisms. The skeletal scheme proposed by the authors takes into account some important reactions that link NO_x to N_2O oxidation, namely:

$$N_2O + O \Longleftrightarrow N_2 + O_2 \tag{6}$$

$$N_2O + O \Longleftrightarrow NO + NO \tag{7}$$

thus providing also a reliable evaluation of N_2O species for H_2-air combustion. Eventually, to give an idea of the impact of hydrogen combustion on the production of the powerful GHG N_2O, two 1D premixed laminar unstretched flames have been calculated at constant burnt gases temperature (T≈1900 K) using the aforementioned detailed kinetic scheme [51]. A comparison has been carried out between CH_4-air and H_2-air reactant mixtures. Global equivalence ratio of ϕ ≈0.6 and 0.7 have been considered, respectively for hydrogen and methane, to keep constant burnt gas temperature. The results show a value of N_2O mass fraction, for hydrogen combustion, doubled compared to methane combustion. Although this is a simplified calculation, it shows what is implied by the widespread use of hydrogen for future aviation and power generation.

When used in AVBP, the reduced skeletal scheme is coupled with simplified constant $Le \neq 1$ transport properties, consisting in determining the viscosity from a power law and deducing the mixture heat conductivity using a constant Prandtl (Pr) number while each species diffusivity relies on a constant Schmidt (Sc) number. This approach often used in LES codes al-

lows to account for differential diffusion between different species. Pr and Sc numbers for each transported species of the mechanism have been optimised in order to fit multicomponent transport and Soret effect. Their values are reported in the Supplementary Materials.

4. Results and discussion

4.1. Cold flow analysis and validation

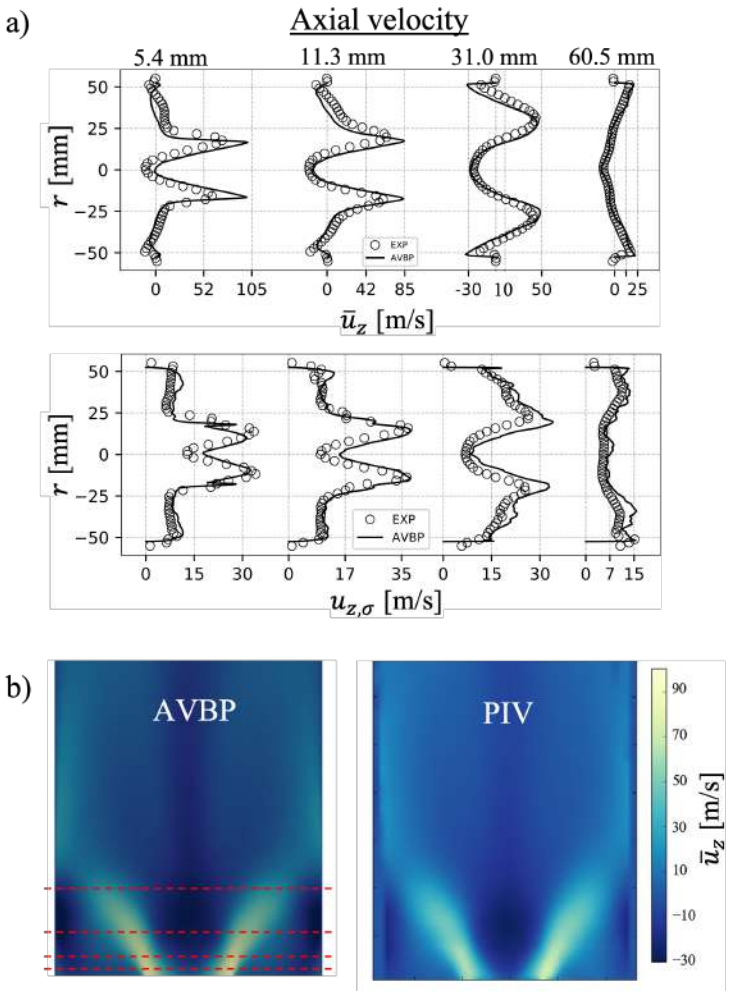

Figure 6: Cold flow - a) Axial velocity ($\bar{u}_z$) and its root mean square ($u_{z,\sigma}$) profiles at different streamwise positions inside the combustion chamber; b) comparison of the mean axial velocity contours calculated with AVBP and experimentally via PIV [63, 30].

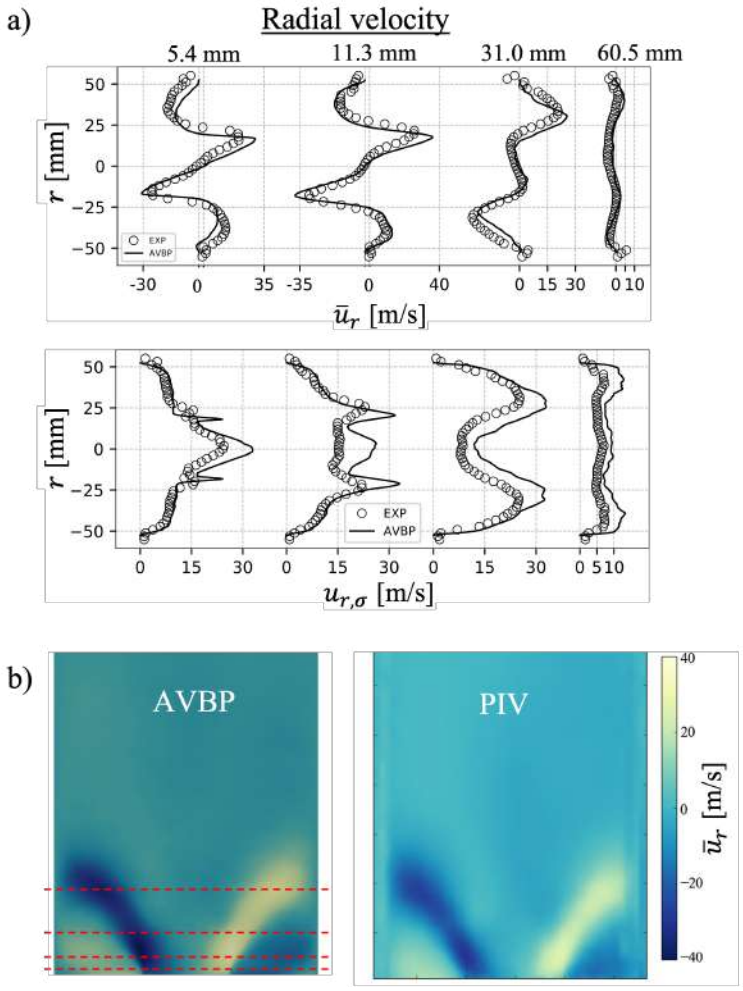

Figure 7: Cold flow - a) Radial velocity ($\bar{u}_{\mathrm{r}}$) and its root mean square ($u_{\mathrm{r},\sigma}$) profiles at different streamwise positions inside the combustion chamber; b) comparison of the mean axial velocity contours calculated with AVBP and experimentally via PIV [63, 30].

As in the experiments, no fuel is considered in the cold flow LES. Time-averaged and root mean square (RMS) profiles of the axial and radial velocity components extracted from an averaged solution (50 ms after initial transition died out) at different locations along the stream-wise direction (5.4,

11.3, 31.0 and 60.5 mm) are compared with experimental PIV data in Fig. 6 and Fig. 7, respectively. The numerical velocity profiles show a good agreement with experiments with some discrepancies in the central part of the recirculation zone close to the backplane (5.4 mm). This can be due to the experimental uncertainties, since measurements of flow velocity components in the proximity of the backplane are a great challenge due to interaction of PIV laser and the walls. The profiles and the levels of RMS are also comparable with experiments. Experimental tangential profiles have not been collected during the experiments, therefore no numerical results have been reported. Finally, the velocity contours indicate that the structure of the recirculation zones and its opening flow angle are in accordance with the experiments.

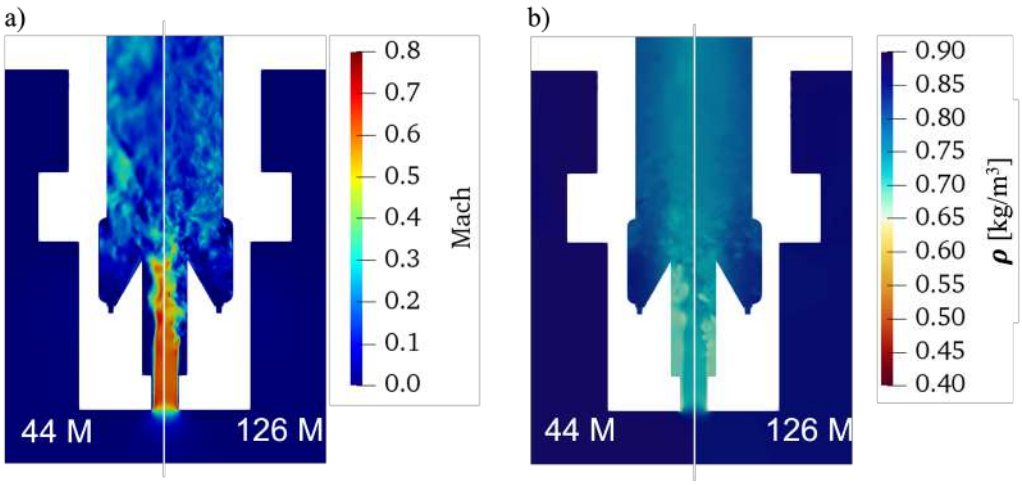

Figure 8: a) Mach number comparison between two different grid refinements; b) density contours comparison between two different grid refinements.

Since this is a technically premixed burner, a large part of the fuel injection system has been modeled, resulting in a more accurate case than

the standard fully premixed case. Due to the complex arrangement of the mixing system (air flow splitting through a swirler and an axial orifice close to the fuel pipes) in this zone, the compressibility effect can affect the mixture formation and its displacement in the tube. This aspect will be further discussed in the following section.

Indeed, Looking at the instantaneous contours of the Mach number in orifice zone, Fig. 8(a), one can see that the flow is slightly below the transonic regime (mean Mach = 0.55), pointing out the importance of solving this case with a compressible solver in contrast with the cases already presented in literature. Compressibility effects can be also discussed by observing the flow density in the orifice region: a density reduction of about 22% is achieved inside the axial passage, Fig. 8(b). Unfortunately, no experimental data are available for a comparison with the actual pressure drop. For this reason, as described in section 3, mesh refinement has been performed in this volume aiming at accurately solving the jet dynamics, the pressure drop, and in return, the air flow splitting rate. In Fig. 8, the field of Mach number is compared for two different grid resolutions. The grid on the left (a coarse mesh with 44 M cells) has been generated with a minimum cell size in the axial duct and mixing tube of 400 μm. On the right, the final grid used for calculations with a refinement up to 250 μm. A grid independence study has been carried out by refining progressively the grid until no substantial variation of the pressure level downstream of the orifice could be recorded. To give an idea of the pressure levels in this region, the pressure has been recorded inside the plenum, at the exit of the orifice and close to the swirler outlet. The average pressure at the exit of the orifice is around 89 kPa with

no remarkable pressure oscillations. Thus, the pressure drop through the orifice (Δp) is of the order of 23 kPa.

The grid size demonstrates to affect the structure of the jet, its length and wrinkling; this also impacts the equivalence ratio distribution in the mixing tube for the successive hot flow simulations. Moreover, looking at the outer radius of the mixing tube, also the flow resolution in this region is clearly improved by reducing the minimum grid size. For the selected operating conditions and diameter of the orifice, the value of air splitting χ obtained by LES without fuel injection (cold case) with Eq. (5) indicates that 14.2% of the flow rate flows through the orifice. The axial flow could change from cold to hot case since the injection of fuel introduces a local pressure reduction and consequently a larger flow rate enters the swirler (χ=13%). Unfortunately, it is not possible to compare these values with experiments, but they are in line with the previous calculations reported by Tanneberger et al. [64].

4.2. Reactive case: mixing process, stable flame analysis and pollutants prediction

After assessing the cold flow simulation, the stable reactive case at global equivalence ratio $\phi = 0.6$ is investigated. As a first step, an analysis of the mixing process is performed to evaluate the spatial mixture distribution before entering the combustion chamber. Eventually, being hydrogen a molecule characterized by peculiar properties, a specific analysis is dedicated to the study of the flame structure and then to the NO_x formation.

4.2.1. Mixing process

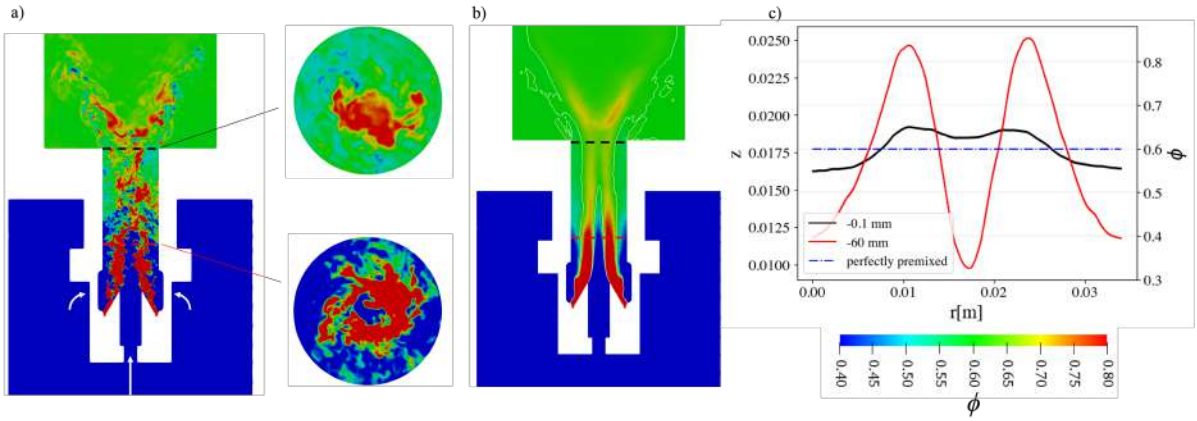

Figure 9: a) Instantaneous field of equivalence ratio, ϕ, in a longitudinal section and in two sections normal to the axial direction; b) Mean field of the equivalence ratio; c) equivalence ratio, ϕ, and mixture fraction, z, profiles along the radial direction inside the tube at two different axial locations.

In Fig. 9(a), an instantaneous plot of equivalence ratio in a longitudinal plane points out the dynamics of the mixing process. The air coming from the swirler (bent white arrows) pushes the fuel coming from the small pipes towards the conical surface. The conical surface borders an axial pipe rim connected to the orifice. In this zone, the mixture is extremely rich. After that, the mixture enters the mixing tube and decelerates. In the first part of the mixing tube, the mixing process is governed by the combination of both the swirling flow and axial jet. A blue gap in the axial region highlights the spatial influence of the axial air jet. An annulus of confined rich mixture is visible on a section at the bottom of the mixing tube, Fig. 9(a). By the half of the tube, the turbulent vortical structures enhance the mixing and in fact contours exhibit a more homogeneous ϕ distribution.

The mean equivalence ratio field is shown in Fig. 9(b) with iso-contours of the global equivalence ratio ϕ=0.6. The mixture close to the walls appears leaner than the global equivalence ratio. The plot on the right illustrates the mixture fraction z (and equivalence ratio ϕ) along the radial direction inside the tube at -60 and -0.1 mm upstream the combustion chamber inlet. The target value is represented by a blue dash dot line. The mixture fraction used in the code is the one defined by Bilger [65]:

$$z = \frac{\beta - \beta_{ox}}{\beta_{fuel} - \beta_{ox}} \tag{8}$$

where *ox* and *fuel* stand for oxidizer and fuel, respectively. In Eq. 8, $\beta = 2Y_C/W_C + 0.5Y_H/W_H - Y_O/W_O$, with Y_i the atomic mass fraction and W_i its molecular weight. In the first part of the mixing tube, the mixture fraction close to the walls is dominated by the swirled air flow; the z deficit in the central part is due to the axial air jet penetration confirming the importance of grid refinement in this zone, Fig. 8. At the end of the mixing zone, the mixture is still lean at outer radii, while it remains slightly rich in the central part. Before entering the combustion chamber, the mixture is not perfectly premixed being the variability of the equivalence ratio in the range $\pm$10% around the global value. This confirms the necessity to take air/fuel injection and the mixing process into account in the numerical model. It can also be said that the length of the mixing tube might have a remarkable impact on the mixture composition at the entrance of the combustion chamber. This results are in line with the experiments performed on the same burner in a water tunnel [17].

4.2.2. Stable flame and impact of the conjugate heat transfer

Previous works on this configuration have been performed by solving the case under adiabatic condition [30]. Thus, in what follows, the importance of considering the thermal boundary conditions via LES-CHT simulations is assessed by comparing adiabatic and non-adiabatic flames. The non-adiabatic case has been studied by applying the methodology described in section 3.2.

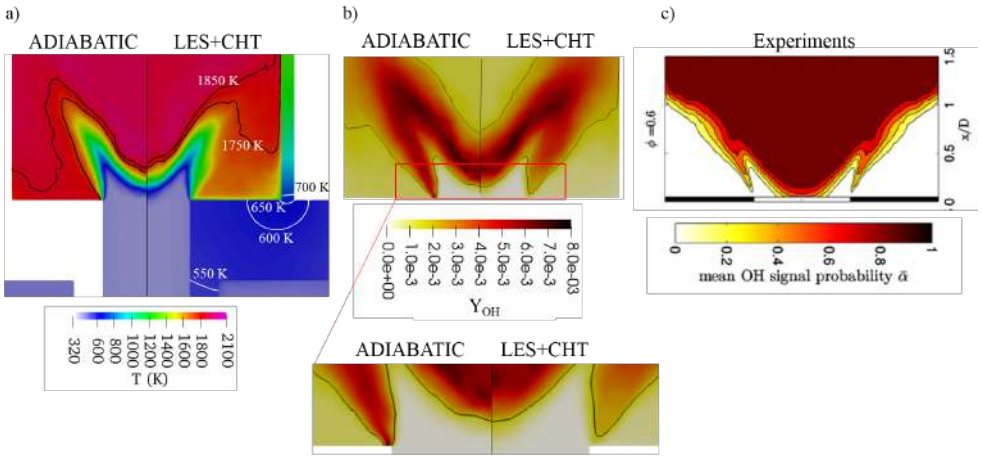

Figure 10: (a) Comparison of temperature [K] field with two iso-contours of temperature, one at T=1850 K and the second at 1750 K. Four iso-curves of temperature in the solid part; (b) Averaged LES contours of OH mass fraction for adiabatic (left half) and CHT (right half) cases, Bottom: enlargement on the anchoring zone to compare adiabatic (left half) and CHT (right half) conditions; (c) experimental OH signal probability [63].

To investigate the impact of the CHT on the flame stabilization and pollutant emissions, a comparison of temperature, heat release rate, NO and N_2O is done for both the adiabatic and LES-CHT cases. As expected, in Fig. 10(a), the temperature field puts in evidence non negligible heat losses at the walls. CHT approach gives access to information on the thermal pattern in the solid, illustrated with iso-contours of T=700, 650, 600 and 550 K drawn

on a slice of the solid domain. The combustion chamber surface, which contains hot gases is responsible for the major part of heat losses. Its walls are heated up to a temperature around 1200 K. Part of this heat diffuses to the backplane leading there to a non uniform radial temperature distribution ranging from 700 K (close to the chamber corner) to 550 K (in proximity of the mixing tube). As this temperature is higher than the flow temperature in the final part of the mixing tube (a value close to the pre-heated air temperature, 453 K), the solid heats back the flow in this zone.

An estimation of the heat transferred through the various solid parts is reported in Tab. 1: a large amount of heat is transferred from the combustion chamber walls to the external ambient, due to the contact of hot gases; the backplane is heated by both the hot gases in the external recirculation zone and by conduction from the combustion chamber walls; finally, heat is redistributed in the plenum volume and go back up to the flow in the mixing tube. The external plenum walls diffuse heat to the external ambient as well, for details refer to section 3.2.

	Combustion chamber	Backplane	Mixing tube
heat transfer [kW]	-14.0	-1.3	0.4

Table 1: Heat transferred through the solid parts: combustion chamber, backplane and mixing tube.

In Fig. 10(b) the averaged OH fields from adiabatic and LES-CHT cases are compared to mean OH signal probability Fig. 10(c) measures [63]. This experimental technique performs an averaged of all the recorded binarized pixelwise snapshots of OH measured by means of OH-PLIF, for more de-

tails refer to [63]. The OH radical delimits the reaction zone with a good accuracy. A M-shape flame is observed in agreement with experiments [63]. Interestingly, the application of the CHT modifies the quantity of OH mass fraction produced improving the agreement with experimental observations: when heat losses are applied the anchoring branches are indeed less intense and detached from the backplane rim (see bottom of Fig. 10). However in both LES, the iso-line of OH mass fraction points out that the central part of the flame is lifted from the backplane line, while the experiments show a high probability to find OH close to the combustion chamber entrance. The authors want to stress that in Fig. 10, the Y_{OH} in a plane is compared with mean OH signal probability measured with OH-PLIF technique. The comparison of these different quantities, the only available in the literature, may be source of uncertainties. Nevertheless, discrepancies of the spatial distribution of OH mass fraction, in proximity of the combustion chamber, can also be due to a likely misleading prediction of axial air jet whose, unfortunately, no experimental data are available.

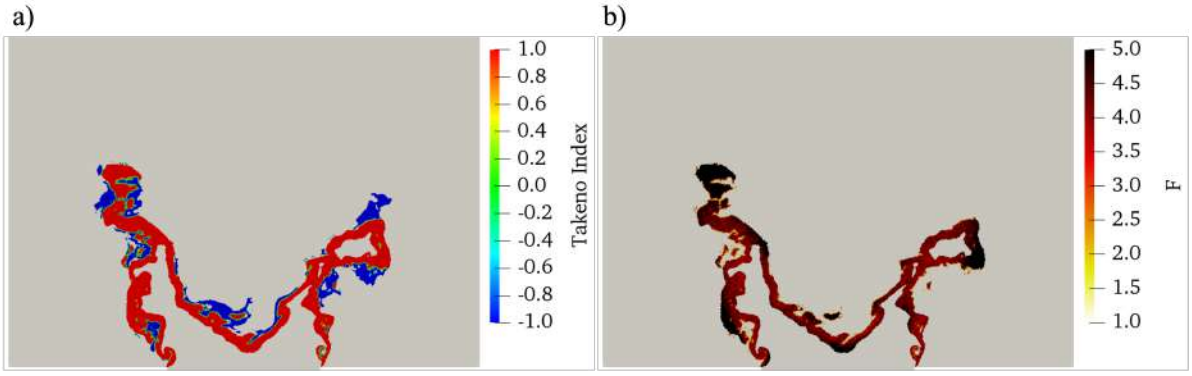

Figure 11: Instantaneous fields of a) Takeno Index and b) thickening factor both conditioned by the HRR.

Continuing the results discussion, an instantaneous plot of the heat release rate (HRR) colored by the Takeno Index (T_I) is represented in Fig. 11(a). The contours reveal a value of T_I=1 in the flame front, thus indicating that the combustion process happens in mainly premixed condition. Nevertheless, diffusion spots are visible in the post flame region (blue spots). Thickening is correctly not applied in those flame regions as confirmed in Fig. 11(b). In Fig. 11(b), the value of thickening factor varies in a range from 1 to 5. In the part of the flame region, it can be observed a value about 4, which is the target value applied during the SMR. The SMR technique is discussed in section 3.1.

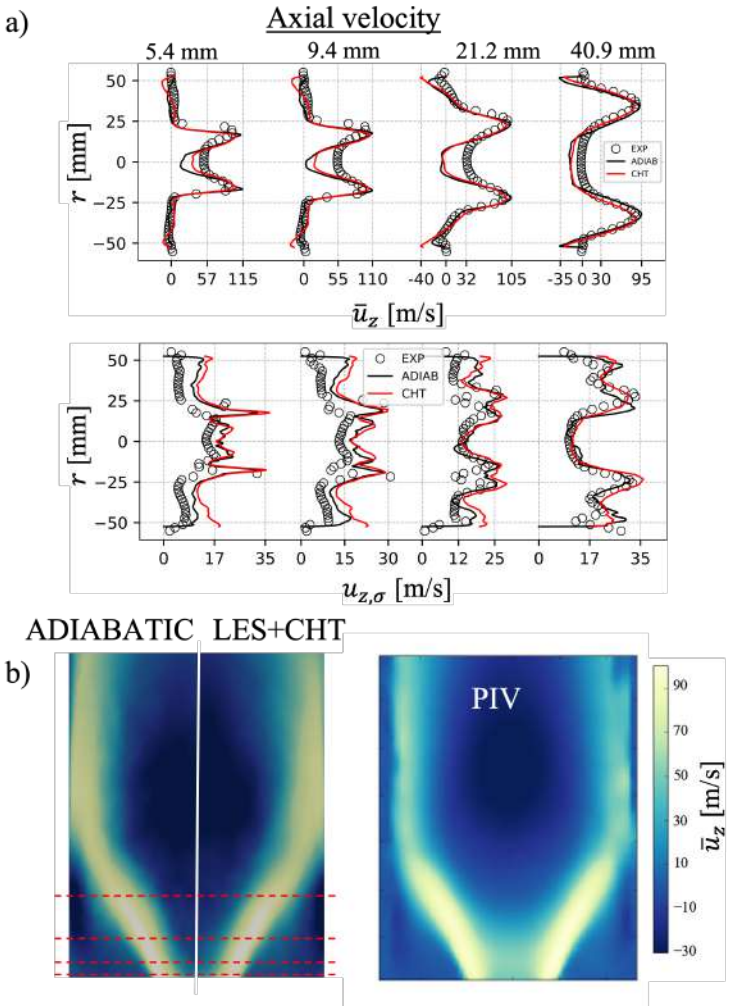

Figure 12: a) Axial velocity ($\bar{u}_z$) and its root mean square ($u_{z,\sigma}$) profiles at different streamwise positions inside the combustion chamber; b) comparison of the mean axial velocity contours calculated with AVBP and experimentally via PIV [63, 30].

The velocity profiles of both adiabatic and LES-CHT cases are compared with PIV data at different locations along the streamwise direction (5.4, 9.4, 21.2 and 40.9 mm) in Fig. 12. The velocity profiles for CHT cases are slightly in better accordance with the experiments. In both cases a little deficit of

the axial velocity is observed in the central recirculation zone, which may be related to the more slightly upstream position of the central flame in the LES, as already seen above. Another source of uncertainties can be the misleading prediction of the axial flow rate jet, in spite of the large number of points used in the mixing zone. Nonetheless, the level of RMS for the axial velocity is comparable between experiments and numerical simulations.

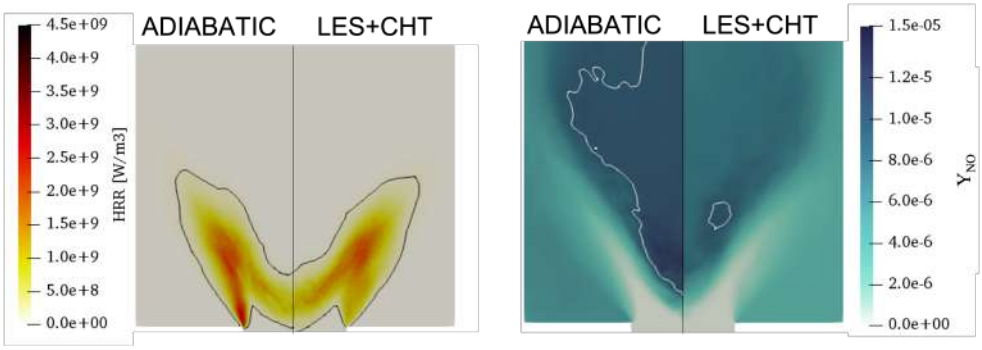

Figure 13: Comparison of the averaged HRR [W/m^3] and NO mass fraction between the adiabatic and non-adiabatic (LES-CHT) cases.

The mean heat release rate distributions (Fig. 13) slightly differ between the adiabatic and non-adiabatic cases, confirming what was already observed from the OH mass fraction field (Fig. 10). Indeed, the adiabatic flame has a high heat release rate close to the backplane, where typically the M-flame is anchored. This is a direct result of the higher flow temperature in the external recirculation zone for the adiabatic case, which is linked to the missing wall heat losses. Since the nature of the Arrenhius law is exponential, the heat losses reduce the reactivity of fresh mixture coming from the mixing tube. A consequence is a slightly narrower central zone of heat release rate in the adiabatic case, as evidenced by the iso-contour at 10^8 W/m^3.

In terms of NO produced by the two models, one can see in Fig. 13 that the higher temperature of the adiabatic case leads to higher value of NO mass fraction, in particular in the central recirculation zone where it is also more uniform. This is highligthed by an isoline at Y_{NO}=1.2e^{-6}. When heat losses are considered, the NO globally decreases and its peak production remains in a limited region close to the inner shear layer zone. To give an idea of the amount of NO_x produced by this burner, two different parameters have been evaluated for the LES-CHT case. The NO_x emission index defined as the mass (in g) of pollutant divided by the mass (in kg) of fuel burned, results here to 0.77 gNO_x/kg$_{fuel}$, and the concentration of NO_x in part per million volume at the gas turbine standard, which is equal to 7 ppmv at 15%O_2 dry. This value is in line with the experiments (7-8.5 ppmv, Fig. 15 in Ref.[63]) confirming the effectiveness of the reduced skeletal kinetic model (H2Air_15_47_TC) in predicting the right level of emission in a real combustor.

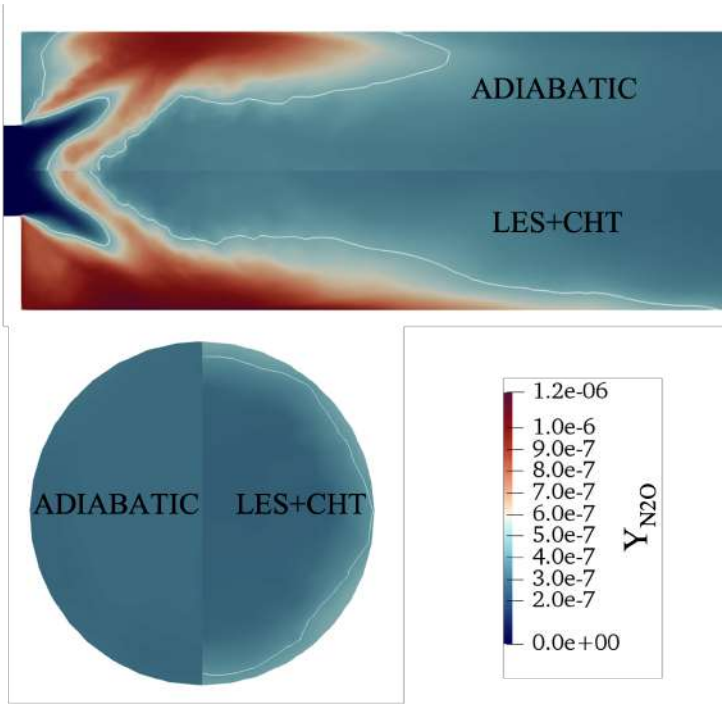

Figure 14: Comparison of the N_2O mass fraction between the adiabatic and non-adiabatic (LES-CHT) cases on a longitudinal plane and on a section normal to the burner axis towards the exit of the combustion chamber.

As discussed in the introduction, an estimation of the amount of N_2O produced during the operation of this burner can be helpful for the future technology development related to hydrogen combustion. The averaged N_2O field is compared between the two cases on a slice in Fig. 14. It is remarkable that the N_2O mass fraction increases close to the walls for the non-adiabatic flame (LES-CHT), as a consequence of the local lower temperature due to heat losses. Looking at a transverse section normal to the burner axis close to the exit of the combustion chamber, a ring of increased N_2O mass fraction can be seen close to the wall where the temperature is reduced in the

non-adiabatic case. The exact chemical process will be detailed in the next section, but few considerations can be done below. The reactions that lead to N_2O formation are easily activated. After that, the abundance of N_2O is converted into NO due to the high temperature (>1800 K). Indeed, comparing Figs. 10(a) and 14, it can be observed that the regions where temperature is lower than 1800 K are the ones where N_2O is not oxidized to NO. For the case studied in this work with the application of the conjugate heat transfer, the N_2O emission index is 0.06 gN_2O/kg_{fuel} and compared to the adiabatic one, it produces +40% of N_2O mass fraction at the exit of the burner.

4.2.3. Differential diffusion effect and analysis of pollutant production

When modeling lean partially premixed hydrogen flames some complexities need to be taken into account. Specifically, being a light molecule, hydrogen tends to fast diffuse and, depending on the flame front wrinkling, regions with hydrogen concentration both over and under the global equivalence ratio can be found. This local variation of the equivalence ratio considerably goes beyond and below the expected values and it impacts on the local flame temperature and finally on the NO_x production. In this section, all these aspects are investigated and the spatial distribution of the radicals and molecules involved in the hydrogen oxidation is analyzed. In particular, the impact of the species production and oxidation is discussed.

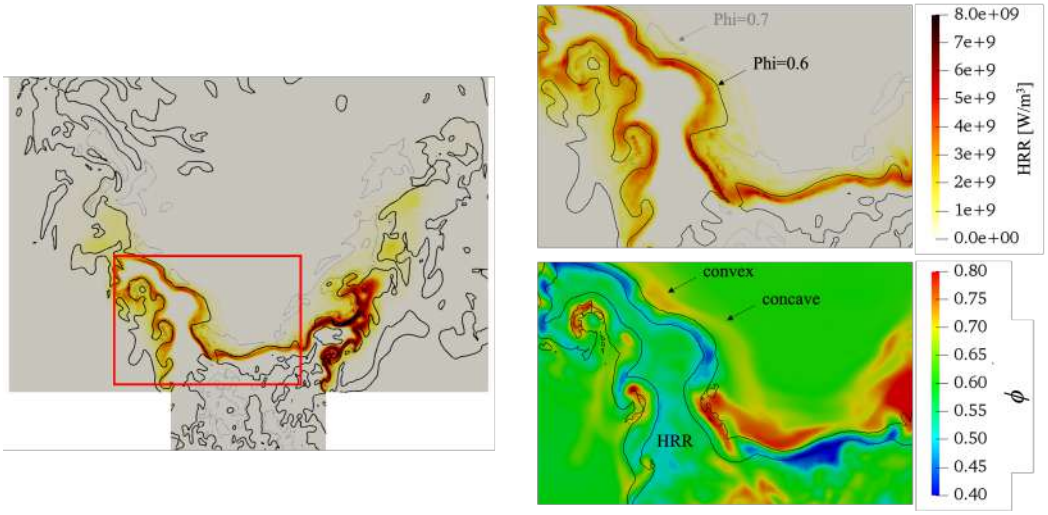

Figure 15: Instantaneous fields of HRR and ϕ in a vertical cut plane for the LES+CHT case, with an isocontour of HRR at 2×10^9 W/m^3. Representation of the concave and convex parts around the flame front.

It is worth to investigate the behaviour of the hydrogen molecules in proximity of the reaction zone which is outlined in Fig. 15 by an iso-contour of heat release rate equal to 2×10^9 W/m^3. A wrinkled surface is observed as expected in regime of turbulent combustion. Due to differential diffusion effects, convex curvatures are prone to accumulate light molecules, such as H_2 and the radical H, whereas, concave surfaces are adjacent to lean mixture spots. This is confirmed by the equivalence ratio contours showing a great variability in this region, but also by the iso-curves in the right upper part of Fig. 15.

As discussed in section 3.3, the NO production in hydrogen combustion involves three different routes: thermal NO, N_2O and NNH. In Fig. 16, a diagram provides an easy representation of the reactions, molecules and atoms involved in this process. This sketch does not want to be exhaustive of all

the species and reaction that play a role in the NO production, but it helps the reader to focus on the chemical processes discussed thereafter.

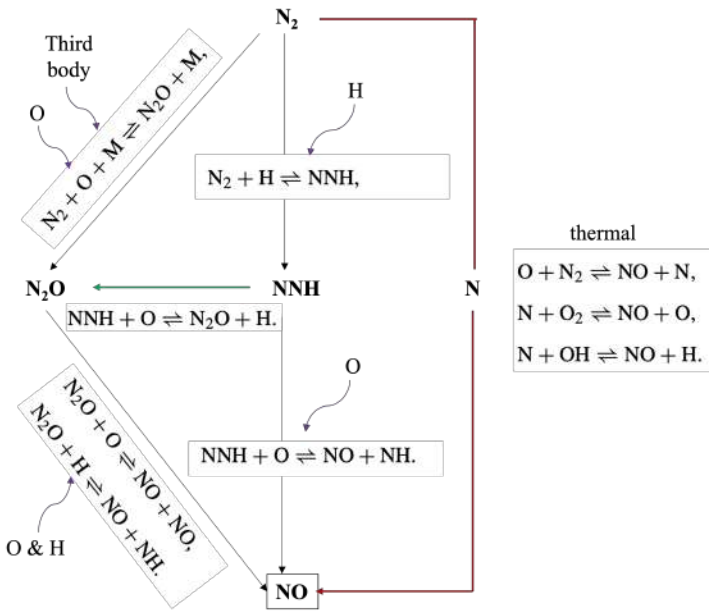

Figure 16: Schematic representation of the pathways, reactions and molecules involved in the NO formation for H_2/air combustion.

Looking at Fig. 15 and 17 some preliminary conclusions need to be addressed. The more or less concentration of H_2 suggests a high energy release and temperature rise, which paves the way to larger thermal NO production compared to a flame front at uniform ϕ.

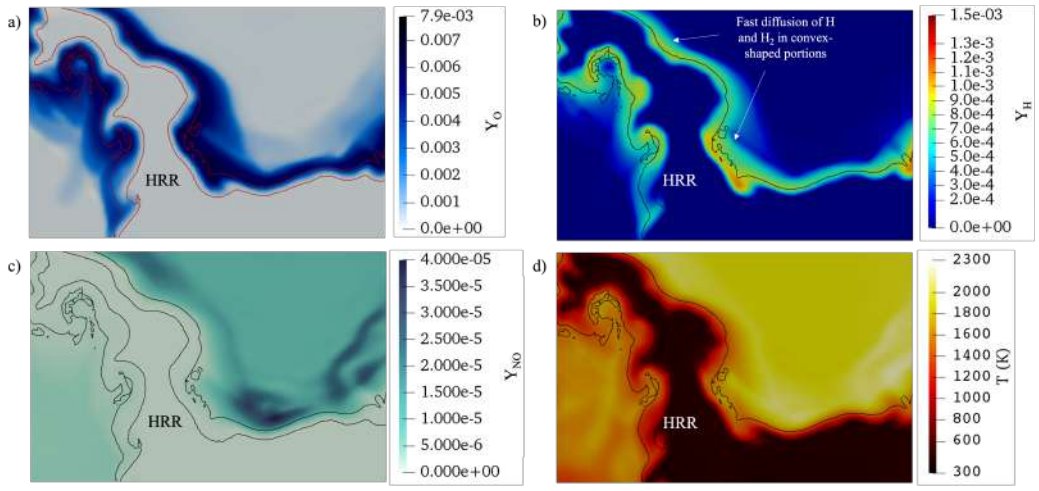

Figure 17: Instantaneous fields of O, H, NO mass fractions and temperature in a vertical cut plane close to the chamber inlet for the LES+CHT case, with an iso-contour of HRR at $2{\times}10^9$ W/m^3.

Figure 17(a) reports an instantaneous field of radical O in proximity of the flame front. It can be seen that this radical is present not only in the post flame region, but peaks are already visible in the reacting zone. This contributes to the thermal NO and N_2O pathways production, and is in line with the conclusions presented by Homer et al. [6], namely, models in which the O production is based on the equilibrium underestimate the final concentration of nitric oxide. The radical O is not affected by fast diffusion, but it favours the low activation energy reaction producing N_2O and successively its oxidation into NO, Fig. 16. Furthermore, O radicals are consumed in other pathways, i.e., the oxidation of NNH either to N_2O or directly to NO.

A speculative analysis can also be made for the light radical H (Fig. 17(b)), formed in the reacting zone. However, since H is a really light atom, it is affected by fast diffusion and it thickens in convex-shaped flame zones. H

atoms give their contribution to the heat release rate through reactions 4 and 20 of the reaction list given in the Supplementary Materials. Looking closely at the iso-curve of heat release rate, where the temperature is around 1600 K, Fig.17(b,d), the presence of radical H promotes the oxidation of N_2 to NNH and the broad atomic oxygen belt complete the process for the oxidation of NNH to N_2O. This process, which is limited to a narrowed region close to the HRR iso-contour, will be evidenced then by the scatter plots in Fig.19. In the regions with an overlap of O and H, the NO contours show a light green zone, Fig.17(c). However, H comes into play in other various oxidation processes either direct or intermediate steps towards the NO production, e.g., thermal and NNH (for instance the fixation of molecular nitrogen to NNH as indicated in Fig. 16), oxidation of N_2O to NO, and the link NNH-N_2O; it is also involved in the formation of other radicals, e.g., OH. Thus, from this qualitative analysis one can not state there is a direct correlation between the preferential diffusion of the radical H and the NO production.

Finally, the contours of NO and temperature (Fig. 17(c-d), respectively) show a good correlation in the peak zones evidencing the high impact of the thermal path when the temperature exceeds the threshold of 1800 K. Thus, it can be stated that for this operating point, the levels of temperature and consequently of NO are mainly controlled by fast diffusion and local increment of equivalence ratio. In the other regions where the temperature is lower, the secondary routes contribute to the fixation of molecular nitrogen and mildly to the NO production.

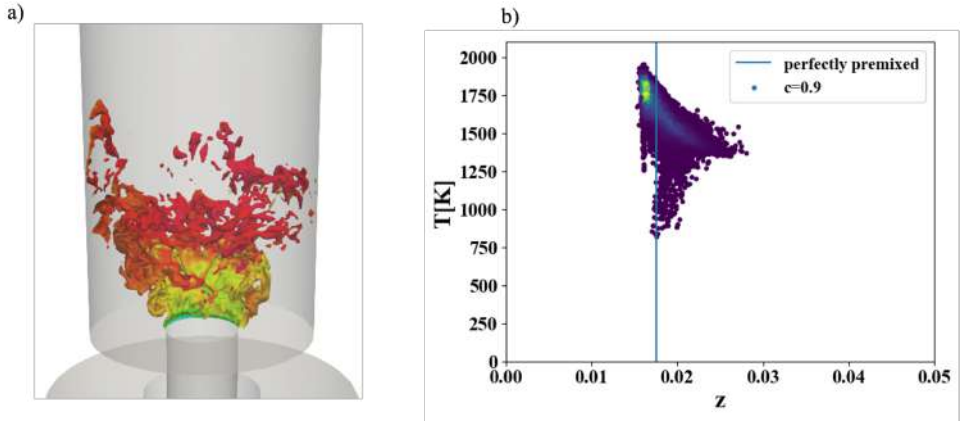

Figure 18: For the LES+CHT case: a) Iso-surface of c=0.9 colored by temperature; b) scatter plot of the temperature as function of the mixture fraction on the iso-c=0.9 colored by a density probability function.

To deepen the NO_x dynamics, scatter plots on instantaneous iso-progress variable (c) surfaces are hereafter discussed. The progress variable is defined as a normalized function of the product H_2O mass fraction. Temperature is firstly investigated in Fig. 18 on a progress variable surface at c=0.9. On the right, the scatter plot of the temperature as function of the mixture fraction on the same surface colored by a probability density function (PDF) evidences the proximity of all the points to the target value represented by a vertical line. The mixture fraction definition used in the code has been defined in Eq. 8. Besides, this plot evidences the importance of two novelties introduced in this work compared to previous ones, firstly the variability of the mixture composition, which is not achievable with a perfectly premixed simulation, and the impact of the heat wall losses on the mixture close to the backplane. The latter parallels what was said about the impact of the heat wall losses on the mixture reactivity, see par. 4.2.2. Two clouds of point can

be detected, one around higher temperature (adiabatic flame temperature of hydrogen at ϕ=0.6) and one around lower temperature (≈1000 K). The latter cloud of points refers to the region close to the backplane, where the reduction of temperature is due to the heat losses.

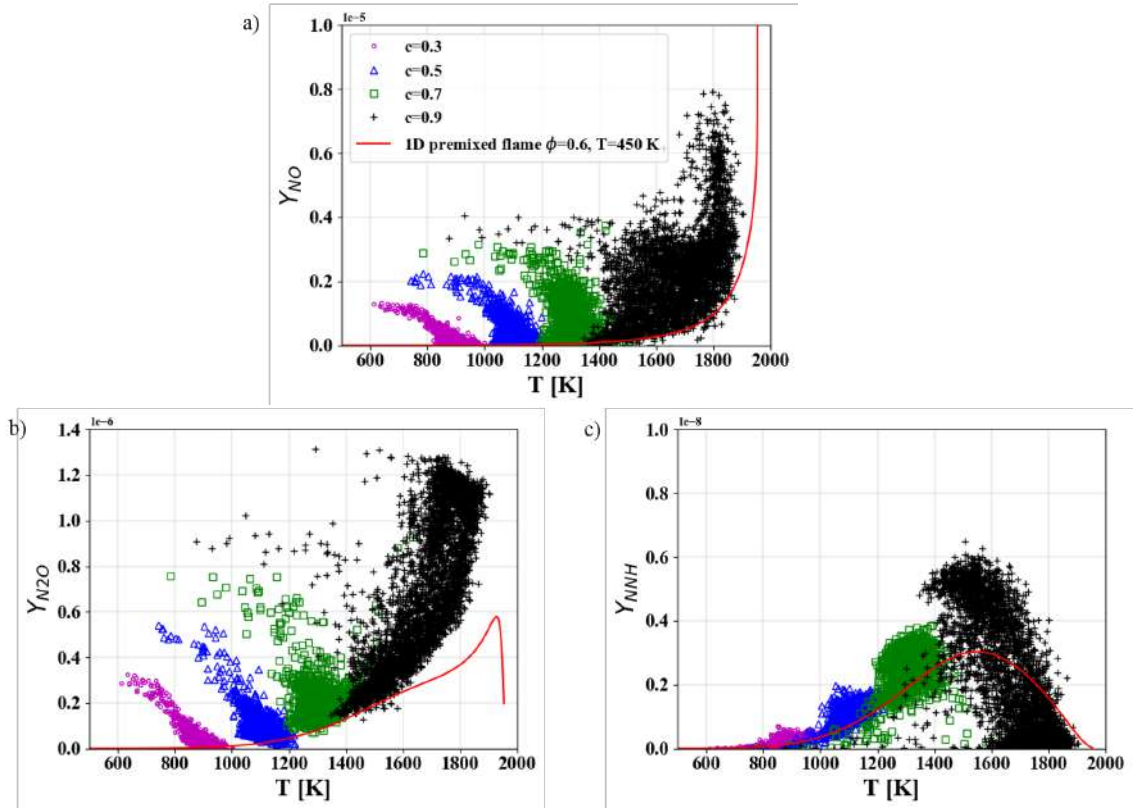

Figure 19: LES+CHT: scatter plots of NO, N_2O and NNH as functions of temperature on different iso-c surfaces: 0.3, 0.5, 0.7, 0.9. The red line corresponds to 1D flame at the same initial temperature and equivalence ratio of the fresh gases.

In order to investigate the effectiveness of the reduced kinetic model used in the present lean hydrogen turbulent flame, several scatter plots of the main species involved in the NO production are proposed. The reader is invited

to refer to Fig. 16 to follow this analysis. In Fig. 19(a), the mass fraction of NO has been plotted on 4 different iso-c surfaces at 0.3, 0.5, 0.7 and 0.9. The NO mass fraction obtained by a 1D perfectly premixed flame calculation with Cantera (www.cantera.org) [61], employing the detailed kinetic scheme (CRECK) at the same initial temperature and global equivalence ratio is superimposed. Overall, the 3D LES scatter results are in line with the 1D cases, even if these exhibit important turbulent dispersion. As expected, thermal NO pathway gains a boost above 1800 K and becomes predominant in the total count.

In Fig. 19(b-c), the same plots have been made for the N_2O and NNH precursors. As it has been observed for NO, the behavior of these species follow the trend predicted by the 1D flame. Moreover, it can be noticed how both N_2O and NNH start growing at T=800 K due to the fixation of N_2 with atomic oxygen and atomic hydrogen. Furthermore, the steep decrease of NNH radical and the fast growth of N_2O suggest that there is a link between these two molecules. This is also evidenced by experiments and analytical models found in the literature [9]. To highlight the associated chemical reaction, mentioned in section 3.3, the scatter plot in Fig. 20 has been added. The hyperbolic trend of this plot means that when NNH is lowest, it has been converted into N_2O through the reaction described in Eq. (5) and vice-versa. Finally, NNH enhances the formation of N_2O then converted into NO by the presence of both H and O in the post flame region, as already shown in the contours in Fig. 17. Only the remaining part of NNH participates directly to the NO production thanks to the thicken layer of O radical, see Figs. 16 and 17.

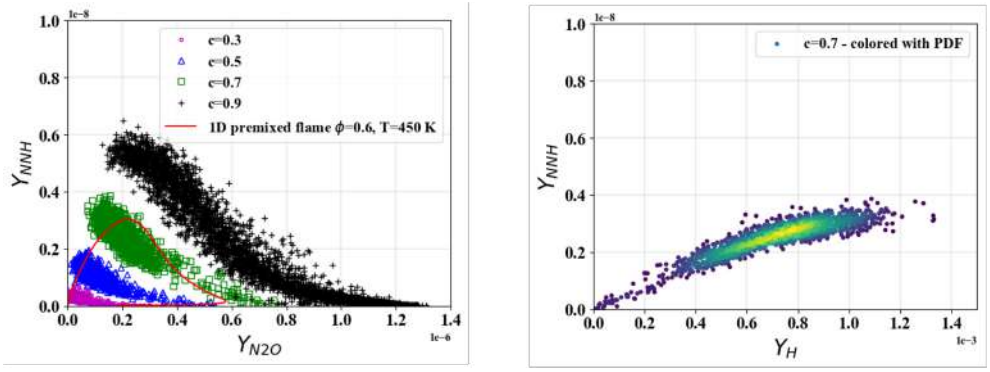

Figure 20: LES+CHT: (left) scatter plots of NNH and N_2O mass fractions on different iso-c surfaces: 0.3, 0.5, 0.7, 0.9., the red line corresponds to 1D flame at the same initial temperature and equivalence ratio of the fresh gases; (right) scatter plot of NNH and H mass fractions on an iso-surface at c=0.7 (right) colored by a probability density function.

The production of NNH and its link to N_2O is pointed out by the scatter plot colored by a probability density function, which correlates the NNH and the H species on an iso-c=0.7 isosurface, Fig. 20(b). Compared to the qualitative previous analysis, the scatter plots provide more qualitative information. Indeed, the fast diffusion of H increase the production of NNH in convex regions of the wrinkled flame. This means that in those regions the NO_x production is not only favored by the high H_2 mass fraction, and consequently by the high temperature, but also by the presence of radicals which slightly enhances the NO oxidation through secondary routes. Given the results, the different order of magnitude of N_2O and NNH mass fraction suggests that NNH formation and destruction is dominated by other reactions, for instance the abstracting of hydrogen by radicals, as indicated by [11].

In the end, LES model with the reduced skeletal kinetic model proposed

in this work (H2Air_15_47_TC) proves to be a reliable tool for the description of complex 3D turbulent flames accounting for preferential diffusion and the prediction of NO_x produced by a H_2-air combustion. Even if only global NO_x data are available on the experimental burner, and no local information can be used for the validation, the good agreement between the LES results and the canonical 1D flames calculated with the detailed kinetic scheme, allows to be confident for further study on premixed and diffusion turbulent flames.

5. Conclusions

The swirled stabilized burner developed at TUB for the combustion of hydrogen-air has been investigated by means of high fidelity compressible LES. To this scope, a new reduced skeletal mechanism (H2Air_15_47_TC) has been developed with ARCANE starting from the detailed scheme proposed by the CRECK modeling group. The reduced skeletal scheme is characterized by 15 species and 47 reactions and has been validated against premixed and diffusion flames available in the literature. Cold flow simulations have been performed paying attention to the axial air jet, designed to contrast flashback, and to the mixing process. Indeed, simulations show that the flow developed inside the orifice is slightly below the transonic regime, thus compressibility effects need to be considered to recover the right mixture formation. Furthermore, a reactive stable case has been investigated (ϕ=0.6). The typical M-flame shape flame has been validated. Both HRR and OH mass fraction fields have been qualitatively compared with experiments. A comparison of the adiabatic and LES-CHT flames has been proposed. This shows the importance to consider the appropriate level of heat boundary

losses in order to capture the right level of temperature in the central and external recirculation zones and consequently the right level of NO_x. In order to study the impact of hydrogen on the flame structure, an analysis has been carried out on the flame front. Convex and concave sections have been detected, pointing out the effect of the preferential diffusion. For lean hydrogen combustion, the fast diffusion of light hydrogen has a large impact on the local temperature and consequently on the NO produced. In this case, the NO is dominated by the thermal pathways. Nonetheless, the analysis of the NO_x formation confirmed the presence of two secondary pathways for the generation of NO_x, one governed by N_2O and one by NNH. The mono directional characteristic of the link between NNH and N_2O and N_2O to NO is conserved. Even if to a small extent, it seems the preferential diffusion of H contributes to the oxidation of NO through secondary routes. Furthermore, due to the low level of NNH, it seems this pathway is conditioned by other reactions such as hydrogen abstracting by radicals. In the end, the numerical set up and the new reduced skeletal scheme demonstrate to be able to capture the right level of NO_x produced by a pure lean hydrogen flame. This paves the way to the application of this methodology with the new skeletal scheme to 3D complex premixed, partially premixed and diffusion flames. In the future, further analyses will be carried out on the relation between turbulence, mixture formation and emissions.

Acknowledgments

This project has received funding from the MIUR under the programme PON AIM (2014-2020 AIM-1883385 CUPD94I18000180007) and H2020 Grant

Agreement 952181 (COEC - Center of Excellence in Combustion). This work was performed using HPC resources from GENCI-TGCC (Grant 2021-A0132B10157).

References

[1] IRENA, Geopolitics of the Energy Transformation: The Hydrogen Factor, International Renewable Energy Agency, Abu Dhabi, 2022.

[2] R. Thompson, L. Lassaletta, P. Patra, C. Wilson, K. Wells, A. Gressent, E. Koffi, M. Chipperfield, W. Winiwarter, E. Davidson, H. Tian, J. Canadell, Acceleration of global N_2O emissions seen from two decades of atmospheric inversion, Nat. Clim. Change 9 (2019) 1–6.

[3] S. Liu, W. Fan, X. Wang, J. Chen, H. Guo, Improvement of kinetic parameters and modeling of the N_2O chemical reaction in combustion, Energy 247 (2022) 123445.

[4] W. Winiwarter, Z. Klimont, The role of n-gases (N_2O, NO_x, NH_3) in cost-effective strategies to reduce greenhouse gas emissions and air pollution in Europe, Curr. Opin. Environ. Sustain. 3 (2011) 438–445.

[5] R. A. Sunyaev (Ed.), 26. Oxidation of Nitrogen in Combustion and Explosions, Princeton University Press, 2014, pp. 404–410.

[6] J. Homer, M. Sutton, Nitric oxide formation and radical overshoot in premixed hydrogen flames, Combust. Flame 20 (1973) 71–76.

[7] P. Glarborg, M. U. Alzueta, K. Dam-Johansen, J. A. Miller, Kinetic modeling of hydrocarbon/nitric oxide interactions in a flow reactor, Combust. Flame 115 (1998) 1–27.

[8] G. J. Rørtveit, J. E. Hustad, S.-C. Li, F. A. Williams, Effects of diluents on NO_x formation in hydrogen counterflow flames, Combust. Flame 130 (2002) 48–61.

[9] M. Skottene, K. E. Rian, A study of NO_x formation in hydrogen flames, Int. J. Hydrogen 32 (2007) 3572–3585.

[10] J. Bozzelli, A. Dean, O + NNH: A possible new route for NO_x formation in flames, Int. J. Chem. Kinet. 27 (1995) 1097–109.

[11] Z.-F. Xu, J.-Z. Sun, Ab initio study on the mechanism of the radical reaction $NNH(^2A')+N(^4S)\rightarrow N_2+NH(^3\Sigma^-)$, Chem. Phys. Lett. 281 (4) (1997) 452–456.

[12] A. L. Purohit, A. Nalbandyan, P. C. Malte, I. V. Novosselov, Nnh mechanism in low-NO_x hydrogen combustion: Experimental and numerical analysis of formation pathways, Fuel 292 (2021) 120186.

[13] P. Glarborg, J. A. Miller, B. Ruscic, S. J. Klippenstein, Modeling nitrogen chemistry in combustion, Prog. Energy Combust. Sci. 67 (2018) 31–68.

[14] A. Durocher, M. Meulemans, P. Versailles, G. Bourque, J. M. Bergthorson, Back to basics – NO concentration measurements in atmospheric lean-to-rich, low-temperature, premixed hydrogen–air flames diluted with argon, Proc. Combust. Inst. 38 (2021) 2093–2100.

[15] R. Cheng, D. Littlejohn, P. Strakey, T. Sidwell, Laboratory investigations of a low-swirl injector with H_2 and CH_4 at gas turbine conditions, Proc. Combust. Inst. 32 (2009) 3001–3009.

[16] G. Oztarlik, L. Selle, T. Poinsot, T. Schuller, Suppression of instabilities of swirled premixed flames with minimal secondary hydrogen injection, Combust. Flame 214 (2020) 266–276.

[17] T. Reichel, S. Terhaar, C. Paschereit, Flow field manipulation by axial air injection to achieve flashback resistance and its impact on mixing quality, Paper No. AIAA 2013-2603, 2013.

[18] N. Tekin, M. Ashikaga, A. Horikawa, D.-I. H. Funke, Enhancement of fuel flexibility of industrial gas turbines by development of innovative hydrogen combustion systems, Gas Energy 2 (2018) 1–6.

[19] M. Rieth, A. Gruber, F. A. Williams, J. H. Chen, Enhanced burning rates in hydrogen-enriched turbulent premixed flames by diffusion of molecular and atomic hydrogen, Combust. Flame 239 (2021) 111740.

[20] A. Aspden, M. Day, J. Bell, Turbulence-chemistry interaction in lean premixed hydrogen combustion, Proc. Combust. Inst. 35 (09 2014).

[21] Y. Minamoto, K. Aoki, M. Tanahashi, N. Swaminathan, DNS of swirling hydrogen–air premixed flames, Int. J. Hydrogen 40 (09 2015).

[22] K. Aoki, M. Shimura, J. Park, Y. Minamoto, M. Tanahashi, Response of heat release rate to flame straining in swirling hydrogen-air premixed flames, Flow Turbul. Combust. 104 (2020) 451–478.

[23] J. Bell, M. Day, M. Lijewski, Simulation of nitrogen emissions in a premixed hydrogen flame stabilized on a low swirl burner, Proc. Combust. Inst. 34 (1) (2013) 1173–1182.

[24] C. Netzer, A. Ahmed, A. Gruber, T. Løvås, Curvature effects on NO formation in wrinkled laminar ammonia/hydrogen/nitrogen-air premixed flames, Combust. Flame 232 (2021) 111520.

[25] M. Gadalla, J. Kannan, B. Tekgül, S. Karimkashi, O. Kaario, V. Vuorinen, Large-eddy simulation of tri-fuel combustion: Diesel spray assisted ignition of methanol-hydrogen blends, Int. J. Hydrogen 46 (2021) 21687–21703.

[26] D. Laera, P. Agostinelli, L. Selle, Q. Cazères, G. Oztarlik, T. Schuller, L. Gicquel, T. Poinsot, Stabilization mechanisms of CH_4 premixed swirled flame enriched with a non-premixed hydrogen injection, Proc. Combust. Inst. 38 (2021) 6355–6363.

[27] P. Agostinelli, D. Laera, I. Chterev, I. Boxx, L. Gicquel, T. Poinsot, On the impact of H_2-enrichment on flame structure and combustion dynamics of a lean partially-premixed turbulent swirling flame, Combust. Flame 241 (2022) 112120.

[28] Y. Afarin, S. Tabejamaat, Effect of hydrogen on H_2/CH_4 flame structure of mild combustion using the les method, Int. J. Hydrogen 38 (2013) 3447–3458.

[29] K. Bioche, L. Bricteux, A. Bertolino, A. Parente, J. Blondeau, Large

eddy simulation of rich ammonia/hydrogen/air combustion in a gas turbine burner, Int. J. Hydrogen 46 (2021) 39548–39562.

[30] D. Mira, O. Lehmkuhl, A. Both, P. Stathopoulos, T. Tanneberger, T. Reichel, C. Paschereit, M. Vázquez, G. Houzeaux, Numerical characterization of a premixed hydrogen flame under conditions close to flashback, Flow Turbul. Combust. 104 (2020) 479–507.

[31] R. Meloni, A. Andreini, P. C. Nassini, A novel LES-based process for NO_x emission assessment in a premixed swirl stabilized combustion system, in: ASME Turbo Expo 2021, Vol. V03AT04A046, Paper No. GT2021-59215, p. 12.

[32] J. Legier, T. Poinsot, D. Veynante, Dynamically thickened flame LES model for premixed and non-premixed turbulent combustion, Proceedings of the Summer Program (01 2000).

[33] F. Duchaine, A. Corpron, L. Pons, V. Moureau, F. Nicoud, T. Poinsot, Development and assessment of a coupled strategy for conjugate heat transfer with large eddy simulation: Application to a cooled turbine blade, Int. J. Heat Fluid Flow 30 (2009) 1129–1141.

[34] N. Franck, F. Ducros, Subgrid-scale stress modelling based on the square of the velocity gradient tensor, Flow Turbul. Combust. 62 (1999) 183–200.

[35] O. Colin, M. Rudgyard, Development of high-order taylor–galerkin schemes for les, J. Comput. Phys. 162 (2000) 338–371.

[36] T. Jaravel, E. Riber, B. Cuenot, G. Bulat, Large eddy simulation of an industrial gas turbine combustor using reduced chemistry with accurate pollutant prediction, Proc. Combust. Inst. 36 (2017) 3817–3825.

[37] B. Rochette, F. Collin-Bastiani, L. Gicquel, O. Vermorel, D. Veynante, T. Poinsot, Influence of chemical schemes, numerical method and dynamic turbulent combustion modeling on LES of premixed turbulent flames, Combust. Flame 191 (2018) 417–430.

[38] F. Charlette, C. Meneveau, D. Veynante, A power-law flame wrinkling model for LES of premixed turbulent combustion part i: non-dynamic formulation and initial tests, Combust. Flame 131 (2002) 159–180.

[39] P. Agostinelli, D. Laera, I. Boxx, L. Gicquel, T. Poinsot, Impact of wall heat transfer in large eddy simulation of flame dynamics in a swirled combustion chamber, Combust. Flame 234 (2021) 111728.

[40] H. Yamashita, M. Shimada, T. Takeno, A numerical study on flame stability at the transition point of jet diffusion flames, Symp. Int. Combust. Proc. 26 (1996) 27–34.

[41] B. Cuenot, F. Shum-Kivan, S. Blanchard, The thickened flame approach for non-premixed combustion: Principles and implications for turbulent combustion modeling, Combust. Flame 239 (2021) 111702.

[42] T. Poinsot, S. Lelef, Boundary conditions for direct simulations of compressible viscous flows, J. Comput. Phys. 101 (1992) 104–129.

[43] B. Kader, Temperature and concentration profiles in fully turbulent boundary layers, Int. J. Heat Mass Transfer 24 (1981) 1541–1544.

[44] W. Agostinelli, B. Rochette, D. Laera, J. Dombard, C. Benedicte, G. Laurent, Static mesh adaptation for reliable large eddy simulation of turbulent reacting flows, Phys. Fluids 33 (2021) 035141.

[45] F. Duchaine, S. Mendez, F. Nicoud, A. Corpron, V. Moureau, T. Poinsot, Conjugate heat transfer with large eddy simulation for gas turbine components, Comptes Rendus Mécanique 337 (2009) 550–561.

[46] F. Duchaine, S. Jauré, D. Poitou, E. Quémerais, G. Staffelbach, T. Morel, L. Gicquel, Analysis of high performance conjugate heat transfer with the openpalm coupler, Comput. Sci. Discov. 8 (2015) 015003.

[47] T. Poinsot, D. Veynante, Theoretical and Numerical Combustion, Edwards, 2005.

[48] J. Grcar, J. Bell, M. Day, The Soret effect in naturally propagating, premixed, lean, hydrogen–air flames, Proc. Combust. Inst. 32 (2009) 1173–1180.

[49] A. L. Sánchez, F. A. Williams, Recent advances in understanding of flammability characteristics of hydrogen, Prog. Energy Combust. Sci. 41 (2014) 1–55.

[50] G. P. Smith, D. M. Golden, M. Frenklach, N. W. Moriarty, B. Eiteneer, M. Goldenberg, C. T. Bowman, R. K. Hanson, S. Song, W. C. Gardiner Jr., V. V. Lissianski, Z. Qin, GRI-Mech, http://combustion.berkeley.edu/gri-mech/.

[51] E. Ranzi, A. Frassoldati, A. Stagni, M. Pelucchi, A. Cuoci, T. Faravelli, Reduced kinetic schemes of complex reaction systems: Fossil and

biomass-derived transportation fuels, Int. J. Chem. Kinet. 46 (2014) 512–542.

[52] C.-W. Zhou, Y. Li, U. Burke, C. Banyon, K. P. Somers, S. Ding, S. Khan, J. W. Hargis, T. Sikes, O. Mathieu, E. L. Petersen, M. AlAbbad, A. Farooq, Y. Pan, Y. Zhang, Z. Huang, J. Lopez, Z. Loparo, S. S. Vasu, H. J. Curran, An experimental and chemical kinetic modeling study of 1,3-butadiene combustion: Ignition delay time and laminar flame speed measurements, Combust. Flame 197 (2018) 423–438.

[53] S. Dong, S. W. Wagnon, L. Pratali Maffei, G. Kukkadapu, A. Nobili, Q. Mao, M. Pelucchi, L. Cai, K. Zhang, M. Raju, T. Chatterjee, W. J. Pitz, T. Faravelli, H. Pitsch, P. K. Senecal, H. J. Curran, A new detailed kinetic model for surrogate fuels: C3mechv3.3, Appl. in En. and Comb. Scien. 9 (2022) 100043.

[54] P. Saxena, F. Williams, Testing a small detailed chemical-kinetic mechanism for the combustion of hydrogen and carbon monoxide, Combust. Flame 145 (2006) 316–323.

[55] P. Boivin, C. Jiménez, A. Sánchez, F. Williams, An explicit reduced mechanism for H_2–air combustion, Proc. Combust. Inst. 33 (2011) 517–523.

[56] M. S. Day, J. B. Bell, X. Gao, P. Glarborg, Numerical simulation of nitrogen oxide formation in lean premixed turbulent $h_2/o_2/n_2$ flames, Proc. Combust. Inst. 33 (1) (2011) 1591–1599.

[57] Q. Cazères, P. Pepiot, E. Riber, B. Cuenot, A fully automatic procedure for the analytical reduction of chemical kinetics mechanisms for computational fluid dynamics applications, Fuel 303 (2021) 121247.

[58] P. Pepiot-Desjardins, H. Pitsch, An efficient error-propagation-based reduction method for large chemical kinetic mechanisms, Combust. Flame 154 (2008) 67–81.

[59] P. Pepiot-Desjardins, H. Pitsch, An automatic chemical lumping method for the reduction of large chemical kinetic mechanisms, Combust. Theory Model. 12 (2008) 1089–1108.

[60] T. Løvås, F. Mauss, C. Hasse, N. Peters, Development of adaptive kinetics for application in combustion systems, Proc. Combust. Inst. 29 (2002) 1403–1410.

[61] D. G. Goodwin, H. K. Moffat, I. Schoegl, R. L. Speth, B. W. Weber, Cantera: An object-oriented software toolkit for chemical kinetics, thermodynamics, and transport processes, https://www.cantera.org, version 2.6.0 (2022).

[62] C. Bowman, R. Hanson, D. Davidson, W. Gardiner, J. Lissianski, G. Smith, D. Golden, M. Frenklach, M. Goldenberg, GRI-Mech2.11, http://combustion.berkeley.edu/gri-mech/.

[63] T. G. Reichel, K. Goeckeler, O. Paschereit, Investigation of lean premixed swirl-stabilized hydrogen burner with axial air injection using OH-PLIF imaging, J. Eng. Gas Turbine Power 137 (2015).

[64] T. Tanneberger, T. G. Reichel, O. Krüger, S. Terhaar, C. O. Paschereit, Numerical investigation of the flow field and mixing in a swirl-stabilized burner with a non-swirling axial jet, in: ASME Turbo Expo 2015, Vol. V04BT04A026, Paper No. GT2015-43382, p. 12.

[65] R. Bilger, S. Stårner, R. Kee, On reduced mechanisms for methane-air combustion in nonpremixed flames, Combust. Flame 80 (1990) 135–149.